GEOPHYSICS, VOL. 83, NO. 1 (JANUARY-FEBRUARY 2018); P. WA49–WA62, 6 FIGS.
10.1190/GEO2017-0065.1

Seismic dispersion and attenuation in saturated porous rocks with aligned fractures of finite thickness: Theory and numerical simulations — Part 1: P-wave perpendicular to the fracture plane

Junxin Guo[1], J. Germán Rubino[2], Nicolás D. Barbosa[3], Stanislav Glubokovskikh[1], and Boris Gurevich[4]

ABSTRACT

When a seismic wave travels through a fluid-saturated porous reservoir containing aligned fractures, it induces oscillatory fluid flow between the fractures and the embedding background medium. Although there are numerous theoretical models for quantifying the associated seismic attenuation and velocity dispersion, they rely on certain assumptions, such as infinitesimal fracture thickness and dilute fracture concentration, which rarely hold in real reservoirs. The objective of this work is to overcome some of these limitations and, therefore, improve the applicability of the available theoretical models. To do so, we extend existing models to the finite fracture thickness case for P-waves propagating perpendicular to the fracture plane using the so-called branching function approach. We consider three types of fractures, namely, periodically and randomly spaced planar fractures, as well as penny-shaped cracks. The extended unified model is then tested by comparing with corresponding numerical simulations based on Biot's theory of poroelasticity. We consider two cases of 2D rock samples with aligned elliptical fractures, one with low fracture density and the other with high fracture density. The results indicate that the influence of the finite fracture thickness on seismic dispersion and attenuation is small at low frequencies when the fluid pressure has enough time to equilibrate between the fractures and background medium. However, this effect is significant at high frequencies when there is not sufficient time for the fluid pressure equilibration. In addition, the theoretical predictions of the penny-shaped crack model are found to match the numerical simulation results very well, even under relatively high fracture density. Analyses of stress distributions suggest that the small discrepancies found between theoretical predictions and numerical simulations are probably due to fracture interactions. In a companion paper, we will extend the analysis for considering the full stiffness matrix and anisotropic properties of such rocks.

INTRODUCTION

The importance of fractures in reservoirs has been recognized for a long time, especially for unconventional and carbonate reservoirs with low matrix permeability (e.g., Kazemi et al., 1976; Abdassah and Ershaghi, 1986; Pérez et al., 1999; Gale et al., 2014; Liu and Abousleiman, 2016; Liu et al., 2017). In many of these reservoirs, the volume of the pores is much larger than that of the fractures, and, hence, the former provides the primary space for hydrocarbon storage (Nelson, 2001). However, due to the very low matrix permeability, fractures provide the main conduits for the flow of pore fluids. Hence, although the total volume of fractures is usually small, their presence can greatly improve the effective permeability of reservoirs and, therefore, hydrocarbon production (Cho et al., 2013). This enhancement of reservoir permeability critically depends on the hydraulic connectivity between the pore space of the background and fractures. Thus, potential seismic information on the connectivity between fractures and pores of the background as well as on the geo-

Manuscript received by the Editor 30 January 2017; revised manuscript received 7 September 2017; published ahead of production 19 October 2017; published online 01 December 2017.
[1]Curtin University, Department of Exploration Geophysics, Perth, Australia. E-mail: junxin.guo@postgrad.curtin.edu.au; stanislav.glubokovskikh@curtin.edu.au.
[2]CONICET, Centro Atómico Bariloche — CNEA, San Carlos de Bariloche, Argentina. E-mail: german.rubino@cab.cnea.gov.ar.
[3]University of Lausanne, Applied and Environmental Geophysics Group, Institute of Earth Sciences, Lausanne, Switzerland. E-mail: nicolas.barbosa@unil.ch.
[4]Curtin University, Department of Exploration Geophysics, Perth, Australia and CSIRO, Kensington, Australia. E-mail: b.gurevich@curtin.edu.au.

metric, mechanical, and hydraulic properties of the probed fractures is of great importance to oil/gas exploration and production.

When a seismic wave propagates through a fractured reservoir that is fully saturated with a single fluid, its behavior can be greatly affected by the properties of the fractures and their degree of hydraulic connectivity with the pore space of the background. This influence results from wave-induced fluid flow (WIFF) between these two regions, a phenomenon highly dependent on the frequency of the elastic wave (Gurevich, 2003). At low frequencies, the pore fluid has enough time to flow from the fractures into the background medium during the compression cycle of the seismic wave and vice versa during the extension cycle, hence reducing the rock stiffness. Conversely, at higher frequencies, there is not sufficient time for fluid flow between the fractures and the background medium. Thus, fractures behave stiffer at higher frequencies than at lower frequencies. The variation of the fracture stiffness with frequency results in frequency-dependent effective elastic properties of the probed fractured material. In other words, fluid flow between the background medium and fractures manifests itself as seismic dispersion, which is accompanied with energy dissipation (seismic attenuation) due to viscous friction arising in the pore fluid.

Seismic dispersion and attenuation due to WIFF between fractures and the background medium have been quantified by several theoretical models. Hudson et al. (1996) model fractures as penny-shaped cracks and quantify the WIFF effects induced by a single crack while neglecting potential interactions with neighboring cracks. Chapman et al. (2002) and Chapman (2003) study the seismic dispersion and attenuation of saturated rocks containing penny-shaped cracks by introducing spherical pores and compliant cracks as perturbations to an elastic nonporous background. Predictions of this model are then compared with the experimental results and applied to seismic data analysis by Maultzsch et al. (2003, 2007) and Chapman et al. (2006). Another perturbation approach to model the effects of pores and fractures on elastic properties is proposed by Jakobsen et al. (2003), Jakobsen and Hudson (2003), and Jakobsen (2004) using a T-matrix formalism. This approach is very versatile because it allows modeling the effect of complex distributions of fractures; however, it depends on many parameters that are often unknown.

A different approach is proposed by Gurevich (2003), who study the effect of fractures in the low-frequency (Gassmann) limit by considering fractures as perturbation to a porous background medium described by Biot's equations of poroelasticity. This work is extended by Brajanovski et al. (2005), who model fractures as thin and highly porous layers embedded in a porous background, based on which an analytical solution for P-wave dispersion and attenuation is obtained. The corresponding characteristic frequencies are also given by studying the asymptotes of the analytical solution at low, intermediate, and high frequencies (Brajanovski et al., 2006). Galvin and Gurevich (2006, 2007) analyze seismic dispersion and attenuation in a medium with aligned sparsely distributed penny-shaped cracks using a poroelasticity approach. A detailed review of these models is given by Gurevich et al. (2009), who also provide a unified formulation for several of these models by using the so-called branching function approach (Johnson, 2001; Pride and Berryman, 2003).

Although numerous theoretical models have been proposed for quantifying seismic dispersion and attenuation as presented above, all of them have simplifying assumptions. For instance, in all these models, the fracture thickness (or fracture volume) is considered infinitesimal. In addition, in some of them, the fracture density should be low enough to ensure that interactions between neighboring fractures are negligible (Hudson et al., 1996; Galvin and Gurevich, 2006, 2007). These assumptions might not hold in real reservoirs, which may limit the applicability of the available models. Some of the assumptions can be overcome by generalizing the existing models, such as in the case of infinitesimal fracture thickness. However, other assumptions, such as dilute fracture concentration, are difficult to overcome. One way to deal with these limitations is to test them using numerical simulations for a given fracture distribution. Indeed, Rubino et al. (2016) proposed a numerical upscaling approach based on Biot's (1941) quasi-static theory of poroelasticity to model seismic dispersion and attenuation of rocks containing arbitrary distributions of fractures. This creates an opportunity to test theoretical models and, in particular, the validity of underlying assumptions.

To expand the applicability of the theoretical models to real fractured reservoirs, two objectives are set in this paper. First, we extend the existing models for infinitesimal-thickness fractures to the case of fractures having finite thickness. Second, numerical simulations are performed to explore the limits of applicability of the derived models. Two 2D numerical rock samples with aligned fractures are studied, one with sparse fracture distribution and the other with dense fracture distribution. The influence of fracture thickness is investigated by comparing the results given by the original models and the extended ones. By contrasting the predictions of the extended models with numerical simulations, we check the correctness of the former and, in addition, we assess the applicability of the theoretical models in rocks with relatively dense fracture concentration. Due to the fact that the dispersion and attenuation of P-waves in the direction perpendicular to the fracture plane are usually much larger than along the other directions (e.g., Galvin and Gurevich, 2015), we focus our analysis on this particular wave mode and propagation direction. In a companion paper (Guo et al., 2017a), we will study the full stiffness matrix of porous rocks with aligned fractures of finite thickness, which can be used to calculate the seismic dispersion and attenuation at any angle of incidence. Furthermore, the velocity and attenuation anisotropic properties of such rocks will also be analyzed. The results will then be compared with the corresponding numerical simulations to check the applicability of the derived theoretical models.

THEORY

Models for fractured rocks with different fracture geometries

In spite of the complex geometries of fractures, for simplicity, they are usually approximated as planes of weakness or penny-shaped cracks. If the radii of the considered fractures are much larger than the predominant seismic wavelengths and fracture spacing, the fractures can be treated as planes of weakness (Gurevich et al., 2009). This means that, in this case, fractures can be represented by highly porous layers (Schoenberg, 1980), which can be called planar fractures. Then, a porous rock with aligned planar fractures can be modeled as layered porous media with infinite lateral extent (Figure 1a). When a seismic wave passes through such a fluid-saturated medium, the pore fluid will flow between the fractures and the background due to the strong stiffness contrast

between these two regions. Hence, seismic dispersion and attenuation will occur and the rock effective elastic properties will become complex-valued and frequency-dependent. If the fractures are distributed periodically in an isotropic background medium, the frequency-dependent saturated P-wave modulus in the direction perpendicular to the fracture plane c^{sat} satisfies (White et al., 1975; Norris, 1993; Brajanovski et al., 2005)

$$\frac{1}{c^{\text{sat}}}=\frac{1}{C_1}+\frac{2}{\sqrt{i\omega\eta}H}\frac{\left(\frac{\alpha_b M_b}{C_b}-\frac{\alpha_c M_c}{C_c}\right)^2}{\sqrt{\frac{M_b L_b}{C_b\kappa_b}}\cot\left(\sqrt{\frac{i\omega\eta C_b}{\kappa_b M_b L_b}}\frac{f_b H}{2}\right)+\sqrt{\frac{M_c L_c}{C_c\kappa_c}}\cot\left(\sqrt{\frac{i\omega\eta C_c}{\kappa_c M_c L_c}}\frac{f_c H}{2}\right)}, \tag{1}$$

where C_b and L_b are the P-wave modulus of the saturated and dry background, respectively; κ_b is the permeability of the background; f_b is the fraction of background with respect to the whole porous medium; $\alpha_b = 1 - K_b/K_{gb}$ is the Biot's coefficient of the background, with K_b being the bulk modulus of the dry background and K_{gb} that of the solid grains composing the background; $M_b = K_{gb}/[(1 - K_b/K_{gb}) - \phi_{bg}(1 - K_{gb}/K_f)]$ is the Biot's modulus of the background, with K_f being the fluid bulk modulus and ϕ_{bg} the porosity of the background. It is interesting to notice that α_b and M_b determine the bulk modulus increment of the background medium due to the fluid saturation ($\Delta K_b = \alpha_b^2 M_b$). The subscript c represents the corresponding values for the fractures. In particular, the Biot's coefficient and modulus for the fracture infill material are $\alpha_c = 1 - K_c/K_{gc}$ and $M_c = K_{gc}/[(1 - K_c/K_{gc}) - \phi_{cg}(1 - K_{gc}/K_f)]$, respectively, with K_c being the bulk modulus of the dry fracture infill material, K_{gc} that of the solid grains composing the fracture infill material, and ϕ_{cg} the porosity of the fracture infill material. In addition, C_1 is the saturated P-wave modulus of the fractured medium in the high-frequency limit of the WIFF, which is computed using the poroelastic Backus average applied to the saturated fractures and background medium [$C_1 = 1/(f_b/C_b + f_c/C_c)$]. The fractures and the background are saturated with the same fluid with shear viscosity η. In addition, ω is the angular frequency of the seismic wave and H represents the spatial period, which is the total thickness of a periodic unit (including the fractures and the background medium).

When the thickness of the planar fractures becomes infinitesimal, equation 1 can be simplified to the following form (Brajanovski et al., 2005; Gurevich et al., 2009):

$$\frac{1}{c^{\text{sat}}}=\frac{1}{C_b}+\frac{\Delta_N\left(\frac{\alpha_b M_b}{C_b}-1\right)^2}{L_b\left[1-\Delta_N+\Delta_N\sqrt{i\Omega}\cot\left(\frac{C_b}{M_b}\sqrt{i\Omega}\right)\right]}, \tag{2}$$

where $\Delta_N = L_b Z_N/(1 + L_b Z_N)$ is the normal fracture weakness, with Z_N being the excess normal compliance induced by the dry fractures, and $\Omega = \omega H^2 M_b \eta/(4\kappa_b C_b L_b)$ is the normalized frequency.

If the radii of the fractures are comparable to or much smaller than their spacing but much larger than the pore size, the fractures can be treated as penny-shaped cracks, which have an oblate spheroidal shape (Figure 1b). For saturated rocks containing aligned penny-shaped cracks, the corresponding seismic dispersion and attenuation due to the WIFF between the fractures and the background medium can be obtained by solving a mixed boundary value problem for Biot's equations of poroelasticity, which is studied by Galvin and Gurevich (2006, 2007) under the assumption that fracture thickness is infinitesimal. The resulting equation for P-waves propagating perpendicular to the fracture plane is an integral equation that requires a numerical solution. However, the asymptotic behavior of the frequency-dependent P-wave modulus at low and high frequencies can be expressed analytically as follows (Galvin and Gurevich, 2006, 2007; Gurevich et al., 2009):

$$\frac{1}{c^{\text{sat}}}=\frac{1}{C_0}\left[1+\frac{i\omega}{D_b}\frac{2M_b(C_b-\alpha_b M_b)^2(2-4\alpha_b g_b+3\alpha_b^2 g_b^2)a^2\varepsilon}{15\mu_b g_b(1-g_b)^2 C_b^2}\right],\quad \omega\ll\omega_c, \tag{3}$$

$$\frac{1}{c^{\text{sat}}}=\frac{1}{C_b}\left[1+\frac{2\sqrt{D_b}\pi\varepsilon(C_b-\alpha_b M_b)^2}{L_b M_b\sqrt{-i\omega}a}\right],\quad \omega\gg\omega_c, \tag{4}$$

where C_0 is the P-wave modulus in the low-frequency limit; μ_b is the dry background shear modulus and g_b is the ratio of μ_b

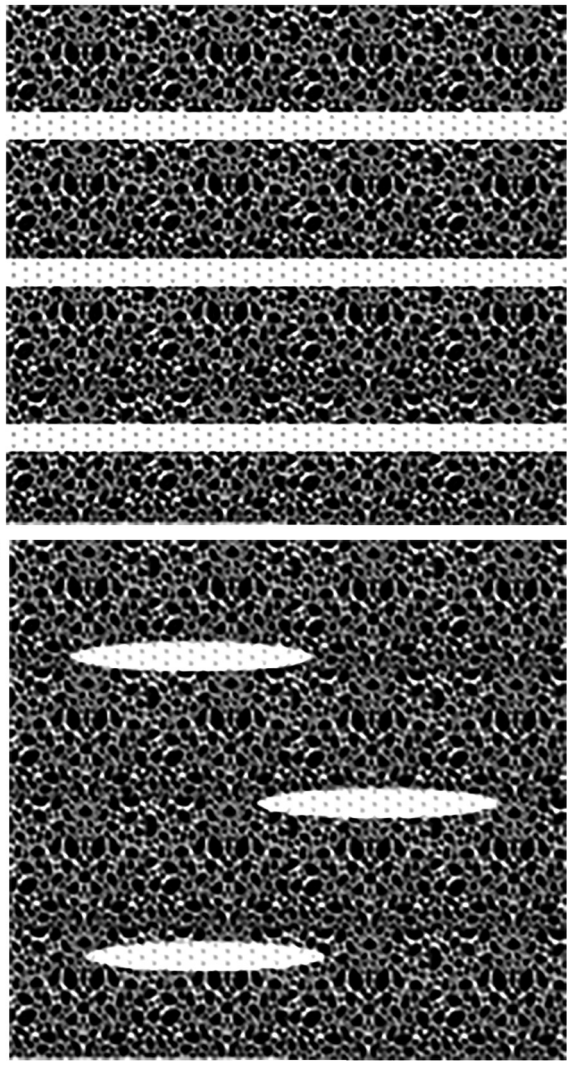

Figure 1. Schematic representation of porous rocks with (a) aligned planar fractures and (b) penny-shaped cracks.

to L_b; a is the radius of the penny-shaped cracks; $\varepsilon = 3f_c/(4\pi\beta)$ is the crack density, with f_c being the fraction of cracks in the rock and β their aspect ratio; $D_b = M_b L_b \kappa_b/(\eta C_b)$ is the hydraulic diffusivity of the saturated background medium; and $\omega_c = 4\pi D_b/a^2$ is the characteristic frequency for the P-wave dispersion and attenuation.

Once the P-wave modulus c^{sat} is computed, combined with the rock density, the phase velocity and attenuation of P-waves in the direction perpendicular to the fracture plane can be obtained (e.g., Carcione, 2001).

Unified model described by branching functions

Gurevich et al. (2009) find that seismic dispersion and attenuation due to the WIFF between the background and the fractures can be presented in a unified form using the so-called branching functions for rocks with aligned planar fractures and penny-shaped cracks. Branching functions are first proposed in the context of WIFF by Johnson (2001) to approximate the frequency-dependent complex stiffness coefficients of porous rocks saturated with a mixture of two fluids. These simple approximations, which have similar behaviors as the asymptotic analytical solutions at low and high frequencies and satisfy causality, turned out to be very accurate and useful. Pride and Berryman (2003) also apply this approach in a medium with a double-porosity structure.

To describe the frequency-dependent P-wave modulus c^{sat} in the direction perpendicular to the fracture plane due to WIFF between the fractures and the background, the following form of branching function is used (Gurevich et al., 2009):

$$\frac{1}{c^{\text{sat}}} = \frac{1}{C_1}\left[1 + \left(\frac{C_1 - C_0}{C_0}\right)\Big/\left(1 - \varsigma + \varsigma\sqrt{1 - i\frac{\omega\tau}{\varsigma^2}}\right)\right], \quad (5)$$

where C_0 and C_1 are the P-wave moduli in the low- and high-frequency limits, respectively, and ζ and τ are the parameters that shape the dispersion and attenuation curves of the elastic coefficient.

At low and high frequencies, equation 5 has the following asymptotes:

$$\frac{1}{c^{\text{sat}}} = \frac{1}{C_0}(1 + i\omega T), \quad \omega\tau \ll \varsigma^2, \quad (6)$$

$$\frac{1}{c^{\text{sat}}} = \frac{1}{C_1}\left(1 + \frac{G}{\sqrt{-i\omega}}\right), \quad \omega\tau \gg 1, \quad (7)$$

where T and G are related to ζ and τ as follows:

$$\tau = \left(\frac{C_1 - C_0}{C_0 G}\right)^2, \quad (8)$$

$$\varsigma = \frac{(C_1 - C_0)^3}{2C_1 C_0^2 T G^2}. \quad (9)$$

Equations 6 and 7 show that seismic dispersion and attenuation caused by WIFF between the fractures and the background is controlled by the parameters T and G together with the elastic properties in the low- and high-frequency limits, C_0 and C_1. In the following, we will first show a method to obtain the expressions of T and G for the infinitesimal thickness case. These expressions will then be extended to the finite fracture thickness case. In addition, expressions for computing the elastic properties in the low- and high-frequency limits will also be given.

Parameters T and G for the infinitesimal fracture thickness case

For the infinitesimal fracture thickness case, Gurevich et al. (2009) derive expressions for the parameters T and G associated with the P-wave modulus in the direction perpendicular to the fracture plane. They are obtained by comparing equations 6 and 7 with the corresponding asymptotic analytical solutions under the limit of infinitesimal fracture thickness. For periodically spaced planar fractures, the low- and high-frequency asymptotes of equation 2 can first be obtained. Then, comparing equations 6 and 7 with these asymptotes yields the following expressions for T and G:

$$T = \frac{1}{12}(C_b - C_0)\frac{Z_N H^2 \eta}{(C_b + Z_N L_b M_b)\kappa_b}, \quad (10)$$

$$G = \frac{2}{H}(C_b - \alpha_b M_b)^2\sqrt{\frac{\kappa_b}{\eta C_b M_b L_b}}. \quad (11)$$

If planar fractures are distributed randomly, numerical simulations indicate that the seismic response at high frequencies is similar to that for the same rock containing the fractures periodically distributed. However, they are different at low frequencies (Lambert et al., 2006). This is due to the fact that the fluid-diffusion length is very small at high frequencies and, hence, the distribution of the fractures has no influence on the seismic properties. Conversely, at low frequencies, the fluid-diffusion length is large and, thus, the seismic dispersion and attenuation will be affected by the fracture distributions. Accordingly, it was found that τ for the random planar fracture case is the same with that for the periodic planar fracture case. However, in contrast to the periodic planar fracture case, ζ equals zero as the effective fracture spacing tends to infinity for random distributions (Gurevich and Lopatnikov, 1995; Müller and Rothert, 2006; Gurevich et al., 2009). Taking this into account, the unified model (equation 5) can be simplified for the random planar fracture case as follows:

$$\frac{1}{c^{\text{sat}}} = \frac{1}{C_1} + \left(\frac{1}{C_0} - \frac{1}{C_1}\right)\Big/\left(1 + \sqrt{-i\omega\tau}\right), \quad (12)$$

where τ is obtained from equation 8 with G shown in equation 11.

For sparsely distributed penny-shaped cracks, the expressions of T and G can be obtained by comparing equations 6 and 7 with equations 3 and 4, which yields

$$T = \frac{2(C_b - \alpha_b M_b)^2(2 - 4\alpha_b g_b + 3\alpha_b^2 g_b^2)a^2\varepsilon\eta}{15\mu_b g_b(1 - g_b)^2 C_b L_b \kappa_b}, \quad (13)$$

$$G = \frac{2\pi\varepsilon}{a}(C_b - \alpha_b M_b)^2\sqrt{\frac{\kappa_b}{\eta C_b M_b L_b}}. \quad (14)$$

Hence, when the fracture thickness is infinitesimal, we can express the P-wave modulus in the direction perpendicular to the fracture plane using the unified model (equation 5) for the three types of fractures considered (periodic planar fractures, penny-shaped cracks, and randomly distributed planar fractures). For different types of fractures, the corresponding expressions of T and G are different, as shown above. Gurevich et al. (2009) show that the results given by the unified model are almost the same with those calculated by the corresponding analytical solutions or numerical simulations, which validates the accuracy of this approach.

It can be noted that for planar fractures and penny-shaped cracks, G can be expressed in the same form as follows:

$$G = 2S(C_b - \alpha_b M_b)^2 \sqrt{\frac{\kappa_b}{\eta C_b M_b L_b}}, \tag{15}$$

where S is called the specific surface area of the fractures per unit volume (Gurevich et al., 2009). For periodic fractures, $S = 1/H$ and for penny-shaped cracks, $S = \pi\varepsilon/a$. Equation 15 implies that at high frequencies, the fluid diffusion length is much smaller than the fracture size and spacing, and therefore, the fluid diffusion and energy dissipation occur in the immediate vicinity of the fracture surfaces, which is controlled by the specific surface area S. This is also supported by numerical simulations (Rubino et al., 2014).

It is important to mention here that the original equations in Gurevich et al. (2009) contain some typographical errors, which are corrected in the equations presented above.

Extension to the finite fracture thickness case

The expressions of T and G given by Gurevich et al. (2009) are for the infinitesimal fracture thickness case. However, all fractures have finite thickness in reality, especially large joints and fracture corridors, which have a particular significant effect on fluid flow (e.g., Questiaux et al., 2010). Hence, it would be useful to extend the unified model (equation 5) to the general case of finite fracture thickness. To do so, we need to obtain the new expressions for T and G considering the finite fracture thickness effects. For periodic planar fracture distributions, this can be done by comparing equations 6 and 7 with the low- and high-frequency asymptotes of the analytical solution for the finite fracture thickness case (equation 1). The low-frequency asymptote of equation 1 is as follows:

$$\frac{1}{c^{\text{sat}}} = \frac{1}{C_0}\left[1 + i\omega \frac{1}{12}\frac{C_1 - C_0}{C_1}\frac{\left(\frac{f_b}{\kappa_b} + \frac{f_c}{\kappa_c}\right)\eta H^2}{\frac{M_b L_b}{C_b f_b} + \frac{M_c L_c}{C_c f_c}}\right]. \tag{16}$$

Comparing equation 16 with equation 6, we can obtain the expression for T for the finite fracture thickness case,

$$T = \frac{1}{12}\frac{C_1 - C_0}{C_1}\frac{\left(\frac{f_b}{\kappa_b} + \frac{f_c}{\kappa_c}\right)\eta H^2}{\frac{M_b L_b}{C_b f_b} + \frac{M_c L_c}{C_c f_c}}. \tag{17}$$

On the other hand, the high-frequency asymptote of equation 1 has the following form:

$$\frac{1}{c^{\text{sat}}} = \frac{1}{C_1}\left[1 + \frac{1}{\sqrt{-i\omega}}\frac{2C_1\left(\frac{\alpha_b M_b}{C_b} - \frac{\alpha_c M_c}{C_c}\right)^2}{H\left(\sqrt{\frac{M_b L_b \eta}{C_b \kappa_b}} + \sqrt{\frac{M_c L_c \eta}{C_c \kappa_c}}\right)}\right], \tag{18}$$

thus giving the expression for G for the finite fracture thickness case as follows:

$$G = \frac{2SC_1\left(\frac{\alpha_b M_b}{C_b} - \frac{\alpha_c M_c}{C_c}\right)^2}{\left(\sqrt{\frac{M_b L_b \eta}{C_b \kappa_b}} + \sqrt{\frac{M_c L_c \eta}{C_c \kappa_c}}\right)}, \tag{19}$$

where $S = 1/H$ is the specific fracture surface area per unit volume for the planar fractures.

If planar fractures are distributed randomly, we can obtain the corresponding expressions for T and G by comparing with the periodic planar fracture distribution case. Because the seismic dispersion and attenuation at high frequencies are independent of the fracture distribution, the parameter G for the random planar fracture distribution case is the same as that for the periodic case (equation 19). At low frequencies, due to the large fluid-diffusion length, seismic dispersion and attenuation will be affected by the fracture distribution, thus making the parameter T for random distribution different from that for the periodic case. As the effective fracture spacing tends to infinity for random distribution of planar fractures, the parameter T will tend to infinity, which corresponds to the zero value for ζ (Gurevich and Lopatnikov, 1995; Müller and Rothert, 2006; Gurevich et al., 2009).

For penny-shaped cracks with finite thickness, due to the fact that at high frequencies energy dissipation only occurs in the immediate vicinity of the fracture surfaces regardless of the fracture types (Rubino et al., 2014), it is reasonable to approximate the expression of G for penny-shaped cracks using that for planar fractures (equation 19). However, the specific fracture surface area per unit volume S is equal to $\pi\varepsilon/a$ for penny-shaped cracks. Furthermore, it can be noted that the properties of the fracture infill material are directly involved in equation 19. Accounting for different geometries between penny-shaped cracks and planar fractures, and considering that the energy dissipation amount is dominated by the compliance contrast between the background and fractures, an equivalent fracture infill material needs to be used in equation 19 for the penny-shaped crack case with finite thickness. This equivalent infill material has the same porosity and permeability with the original infill material of penny-shaped cracks, but has different elastic properties as follows (Brajanovski et al., 2005):

$$L_c = \frac{f_c}{Z_N}, \tag{20}$$

$$\mu_c = \frac{f_c}{Z_T}, \tag{21}$$

where Z_N and Z_T are the normal and tangential excess compliances of the dry penny-shaped cracks, respectively, and L_c and μ_c are the effective P-wave and shear moduli of the equivalent fracture infill material. The values of L_c and μ_c can then be used to calculate the Biot's coefficient and modulus α_c and M_c, and also the saturated P-wave modulus C_c for the equivalent fracture infill material. The values of G for the penny-shaped crack case can thus be obtained

from equation 19 with the specific surface area of the penny-shaped cracks.

At low frequencies, Galvin and Gurevich (2009) show that the attenuation of saturated rocks with a sparse distribution of aligned penny-shaped cracks is not sensitive to the crack thickness. Even the differences between the attenuation for saturated rocks with aligned penny-shaped cracks of infinitesimal thickness and that for the rocks with spheres of the same radius are very small at low frequencies. Because the attenuation at low frequencies is determined by the parameter T as shown in equation 6, the crack thickness should have little effect on this parameter. Hence, we can use the same expression of T for the penny-shaped cracks with finite thickness as that for infinitesimal thickness (equation 13).

Thus, we have extended the expressions of T and G to the case with finite fracture thickness for rocks with planar fractures (periodically or randomly distributed) and penny-shaped cracks. It can be noted that, when the fracture thickness tends to infinitesimal, these extended expressions will reduce to those for the infinitesimal thickness case, which supports the goodness of our extension.

Elastic properties in the low- and high-frequency limits

The elastic properties in the low- and high-frequency limits, C_0 and C_1, are needed for computing the branching functions for the infinitesimal and finite fracture thickness cases. These values can be calculated using the linear slip theory (e.g., Schoenberg and Sayers, 1995) and Gassmann's equations (e.g., Gassmann, 1951) regardless of the fracture geometries (planar fractures or penny-shaped cracks) (Gurevich, 2003; Gurevich et al., 2009). To do so, we need to obtain the dry fracture compliances first. To include the finite fracture thickness effect and specify different fracture geometries, we use the full Eshelby solution instead of popular effective medium theories based on penny-shaped crack geometries. Hence, the compliances of the dry fractures considering finite fracture thickness effect are calculated as follows (Sevostianov and Kachanov, 1999):

$$\mathbf{F} = f_c[(\mathbf{T_c} - \mathbf{T_b})^{-1} + \mathbf{Q}]^{-1}, \tag{22}$$

where $\mathbf{F}$ is the dry fracture excess compliance tensor; $\mathbf{T_c}$ and $\mathbf{T_b}$ are the compliance tensors of the dry fracture filling material and the dry background medium, respectively; and $\mathbf{Q}$ can be obtained from the stiffness tensor of the dry background medium $\mathbf{C}$ and the Eshelby's tensor $\mathbf{S}$ as follows:

$$Q_{ijkl} = C_{ijmn}(J_{mnkl} - S_{mnkl}), \tag{23}$$

where $\mathbf{J}$ is the unit fourth rank tensor; the expressions of Eshelby's tensor $\mathbf{S}$ are shown in Appendix A. Once $\mathbf{F}$ is computed, it can be condensed into the Voigt matrix form $\mathbf{Z}_0$ (Nye, 1985).

For the infinitesimal fracture thickness case, there are only one normal and two tangential nonzero dry fracture compliances, whereas the other components of the dry fracture compliance matrix are equal to zero (Galvin and Gurevich, 2015). Schoenberg and Douma (1988) show that the finite fracture thickness effect on the dry normal and tangential fracture compliances is small for small aspect ratios ($\beta < 0.1$). Hence, for the infinitesimal fracture thickness case, we use the same formula (equation 22) as that for the finite fracture thickness case to calculate the dry normal and tangential fracture compliances.

For computing the response in the low-frequency limit, we first obtain the elastic properties of the dry fractured rock using the linear slip theory (Schoenberg and Sayers, 1995):

$$\mathbf{S}_d = \mathbf{S}_b + \mathbf{Z}_0, \tag{24}$$

where $\mathbf{S}_d$ and $\mathbf{S}_b$ are the compliance matrices of the dry fractured rock and the dry background medium, respectively, and $\mathbf{Z}_0$ is the dry fracture compliance matrix. The stiffness matrix $\mathbf{C}_d$ of the considered dry fractured rock can thus be obtained by taking the inverse of $\mathbf{S}_d$.

Then, the elastic properties of the saturated sample in the low-frequency limit can be obtained using the anisotropic Gassmann equation (Gassmann, 1951; Brown and Korringa, 1975; Gurevich, 2003) as the fluid pressure is uniform throughout the considered rock:

$$c^{\mathrm{sat}}_{ij,lf} = c^d_{ij} + \alpha_i \alpha_j M_d, \quad i,j = 1, \ldots, 6, \tag{25}$$

where c^d_{ij} is the corresponding component of $\mathbf{C}_d$, α is the Biot's coefficient, which takes the following form:

$$\alpha_m = 1 - \frac{\sum_{n=1}^{3} c^d_{mn}}{3K_g}, \tag{26}$$

for $m = 1$, 2, and 3, $\alpha_4 = \alpha_5 = \alpha_6 = 0$, and M_d is the Biot's modulus:

$$M_d = \frac{K_g}{(1 - K^*_0/K_g) - \phi(1 - K_g/K_f)}. \tag{27}$$

In equation 27, ϕ is the overall rock porosity and K^*_0 represents the generalized drained bulk modulus defined as follows:

$$K^*_0 = \frac{1}{9}\sum_{i=1}^{3}\sum_{j=1}^{3} c^d_{ij}. \tag{28}$$

It should be noted that, for fractures with infinitesimal thickness, fracture porosity (with respect to the whole rock) is negligible and hence ϕ only contains the porosity of the background medium. Conversely, for fractures with finite thickness, the fractures contribute to the overall porosity of the rock and hence ϕ includes the porosities of the background medium and the fractures.

In the high-frequency limit, the fractures are hydraulically isolated from the saturated background medium. Hence, the saturated fractured medium can be treated as the saturated background permeated by the hydraulically isolated saturated fractures. The elastic properties of the saturated background can be obtained using the isotropic Gassmann's equation as follows:

$$K^{\mathrm{sat}}_b = K_b + \alpha_b^2 M_b, \tag{29}$$

$$\mu^{\mathrm{sat}}_b = \mu_b, \tag{30}$$

where K^{sat}_b and μ^{sat}_b are the bulk and shear moduli of the saturated background medium, respectively. The stiffness matrix of the saturated background medium $\mathbf{C}^{\mathrm{sat}}_b$ can thus be calculated.

For the case of infinitesimal fracture thickness, the compliance matrix of the hydraulically isolated fractures $\mathbf{Z}_1$ has the same values of the tangential fracture compliances as those of the dry fracture matrix $\mathbf{Z}_0$. However, the normal fracture compliance reduces to zero due to the infinitesimal fracture thickness (Galvin and Gurevich, 2015). Hence, $\mathbf{Z}_1$ can be obtained and the elastic properties of the saturated rocks with aligned fractures of infinitesimal thickness in the high-frequency limit can be calculated using the linear slip theory as follows:

$$\mathbf{S}_{hf}^{\text{sat}} = \mathbf{S}_{b}^{\text{sat}} + \mathbf{Z}_1, \tag{31}$$

where $\mathbf{S}_{hf}^{\text{sat}}$ is the compliance matrix of the saturated fractured rocks in the high-frequency limit, and $\mathbf{S}_{b}^{\text{sat}}$ is the compliance matrix of the saturated background medium, which can be obtained by taking the inverse of $\mathbf{C}_{b}^{\text{sat}}$. The stiffness matrix $\mathbf{C}_{hf}^{\text{sat}}$ of the saturated fractured rocks can then be computed from $\mathbf{S}_{hf}^{\text{sat}}$.

For the case with finite fracture thickness, the tangential fracture compliances in the high-frequency limit are similar to those for the dry fractures. However, the other nonzero components in the fracture compliance matrix do not vanish but have small finite values (Gurevich, 2003). Under this condition, the elastic properties of the saturated fractured rock in the high-frequency limit can be obtained as follows. First, we obtain the compliance matrix of the saturated background medium permeated by the dry fractures $\mathbf{S}_{hf}^{1}$ using the linear slip theory:

$$\mathbf{S}_{hf}^{1} = \mathbf{S}_{b}^{\text{sat}} + \mathbf{Z}_0. \tag{32}$$

Then, the stiffness coefficients of the saturated fractured rock $c_{ij,hf}^{\text{sat}}$ can be obtained by saturating the dry fractures with fluid using the anisotropic Gassmann equation (Gurevich, 2003):

$$c_{ij,hf}^{\text{sat}} = c_{ij,hf}^{1} + \alpha_i^1 \alpha_j^1 M_1, \quad i,j = 1,\ldots,6, \tag{33}$$

where $c_{ij,hf}^{1}$ is obtained by taking the inverse of $\mathbf{S}_{hf}^{1}$, α^1 is the corresponding Biot's coefficient, which has nonzero values for $i = 1$, 2, 3 and can be expressed as follows:

$$\alpha_i^1 = 1 - \frac{\sum_{j=1}^{3} c_{ij,hf}^{1}}{3K_b^{sat}}, \tag{34}$$

and M_1 is the corresponding Biot's modulus, which can be written as follows:

$$M_1 = \frac{K_b^{\text{sat}}}{(1 - K_1^*/K_b^{\text{sat}}) - \phi_c(1 - K_b^{\text{sat}}/K_f)}, \tag{35}$$

where $\phi_c = f_c\phi_{cg}$ is the fracture porosity with respect to the whole rock; K_1^* is the generalized bulk modulus, which can be calculated from equation 28 by replacing c_{ij}^{d} with $c_{ij,hf}^{1}$.

With the expressions obtained for the parameters involved in the branching function presented above, we can use equation 5 for computing the frequency-dependent P-wave modulus in the direction perpendicular to the fractures for infinitesimal and finite fracture thickness cases.

NUMERICAL SIMULATIONS

An alternative approach for computing the effective seismic properties of fluid-saturated porous rocks containing fractures consists in the application of upscaling procedures based on numerical oscillatory relaxation tests. The fractures are represented as highly compliant, highly porous, and highly permeable heterogeneities embedded in a much stiffer and much less porous and permeable background. By solving the poroelastic equations under appropriate boundary conditions, the volume average stress and strain components in response to the applied tests are inferred for a representative synthetic rock sample. These parameters then allow for evaluating effective complex-valued, frequency-dependent stiffness coefficients. This kind of numerical approach does not suffer from the limitations of the theoretical models, such as low fracture density or infinitesimal fracture thicknes, which makes them very useful for testing the applicability of the latter.

A defining characteristic of fractured media is that they tend to exhibit pronounced seismic anisotropy, which, in general, cannot be accounted for by classical isotropic upscaling approaches or their high-symmetry anisotropic extensions (e.g., Rubino et al., 2009; Wenzlau et al., 2010). To overcome this limitation, Rubino et al. (2016) developed a novel upscaling approach, which allows for estimating the seismic properties of 2D heterogeneous fluid-saturated porous media in the presence of generic effective anisotropy. In this work, we use this methodology and, mainly due to the high computational cost, we limit the analysis to 2D cases and compare with theoretical results for the corresponding 3D samples under the plane-strain condition.

Following Rubino et al. (2016), we apply three oscillatory relaxation tests on a square sample that is representative of the fractured formation of interest. First, we apply homogeneous time-harmonic normal displacements on the top and bottom boundaries of the sample, while the lateral boundaries are confined. Because we are interested in the undrained response, the fluid is not allowed to flow into or out of the sample. Next, a similar test similar is applied, but the normal displacements are applied on the lateral boundaries of the sample. Finally, we apply a simple shear to the probed fractured rock.

To obtain the response of the sample subjected to the relaxation tests, we solve Biot's (1941) consolidation equations under corresponding boundary conditions. The reasoning behind this is that for frequencies much lower than Biot's characteristic frequency and low enough so that the involved seismic wavelengths are much larger than the size of the heterogeneities, WIFF is Poiseuille type and inertial effects can be neglected. Locally, the total stress equilibrium and Darcy's law are then to be fulfilled simultaneously, which in 2D and in the space-frequency domain yield:

$$\nabla \cdot \boldsymbol{\sigma} = 0, \tag{36}$$

$$i\omega \frac{\eta}{\kappa}\mathbf{w} = -\nabla p_f, \tag{37}$$

where $\boldsymbol{\sigma}$ is the total stress tensor, p_f is the fluid pressure, $\mathbf{w}$ is the average relative fluid displacement, and κ is the rock permeability.

Next, for each kth oscillatory test described above ($k = 1$, 2, 3), we compute the volume averages of the strain and stress components:

$$\langle \varepsilon_{ij}^k \rangle = \frac{1}{V} \int_\Omega \varepsilon_{ij}^k dV, \tag{38}$$

$$\langle \sigma_{ij}^k \rangle = \frac{1}{V} \int_\Omega \sigma_{ij}^k dV, \tag{39}$$

where $\boldsymbol{\varepsilon}_{ij}$ are the components of the stress tensor and Ω is the domain of volume V that represents the probed sample. Assuming that the average behavior of the probed fractured rock can be represented by an equivalent homogeneous anisotropic viscoelastic solid, the average strain and stress components can be related through a complex-valued frequency-dependent equivalent Voigt stiffness matrix $\mathbf{C}$:

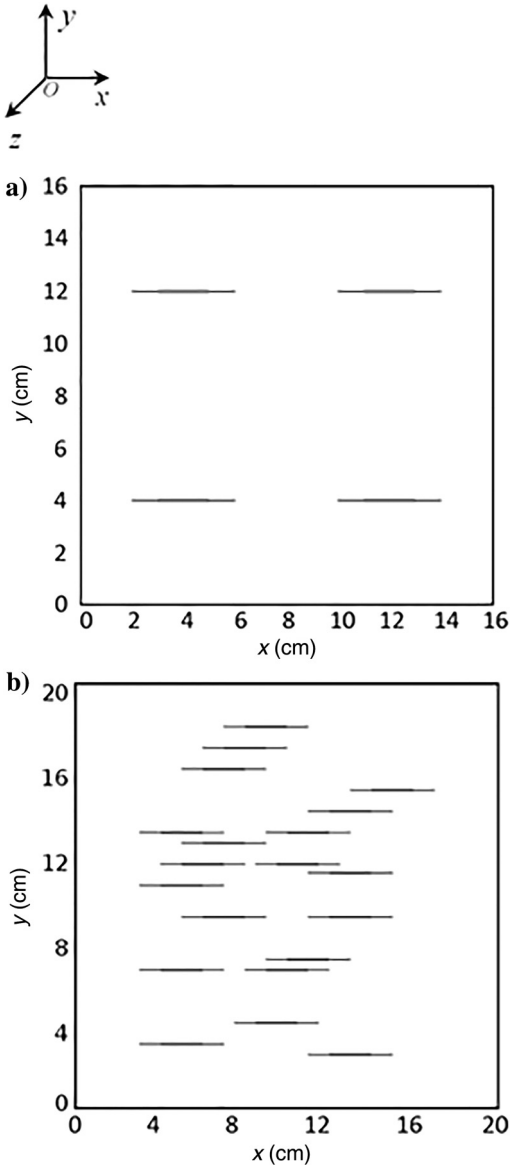

Figure 2. Two-dimensional synthetic rock samples investigated. (a) Sample with four parallel fractures. (b) One realization of samples with 20 parallel fractures randomly distributed.

$$\begin{pmatrix} \langle \sigma_{11}^k \rangle \\ \langle \sigma_{22}^k \rangle \\ \langle \sigma_{12}^k \rangle \end{pmatrix} = \begin{pmatrix} C_{11} & C_{12} & C_{16} \\ C_{12} & C_{22} & C_{26} \\ C_{16} & C_{26} & C_{66} \end{pmatrix} \begin{pmatrix} \langle \varepsilon_{11}^k \rangle \\ \langle \varepsilon_{22}^k \rangle \\ \langle 2\varepsilon_{12}^k \rangle \end{pmatrix}. \tag{40}$$

Equation 40 holds for the three oscillatory tests described above. Therefore, we establish nine equations, and the six unknown stiffness coefficients are computed using a classic least-squares algorithm.

It is important to note here that because we only consider the seismic dispersion and attenuation due to the WIFF between the fractures and the background medium, the theoretical predictions and the numerical simulations are only valid in the frequency range that is much lower than the Biot's characteristic frequency ω_B. It means the effect of the inertial forces is negligible and the WIFF is Poiseuille flow. In addition, the frequencies are also low enough so that the seismic wavelength is much larger than the size of the heterogeneities, which ensures that the effective medium approach is still valid. Hence, for the frequency range considered in this paper, low frequencies refer to the frequencies at which the fluid pressure in the fractures has enough time to equilibrate with that in the background medium within a half-wave cycle. Conversely, high frequencies mean that there is not sufficient time during a half-wave cycle for fluid-pressure communication between the two regions.

COMPARISON BETWEEN THEORETICAL PREDICTIONS AND NUMERICAL SIMULATIONS

Parameters of the investigated sample

We first study one synthetic 2D rock sample with low fracture density, as shown in Figure 2a. It is a square rock of 16 cm side-length and contains four parallel regularly distributed fractures, that is, the fracture density considered in this case is approximately 0.06. The coordinate system is chosen such that the fractures are parallel to the x-axis and perpendicular to the y-axis (Figure 2). The length of the sample along the z-axis is long enough to make sure that the normal and shear strains along this direction are negligible compared with those along the x- and y-axes. Thus, the plane-strain condition is satisfied, which simplifies the 3D problem into a 2D problem.

The properties of the background medium are as follows (Rubino et al., 2015): grain bulk modulus $K_{gb} = 37$ GPa, dry background bulk modulus $K_b = 26$ GPa, shear modulus $\mu_b = 31$ GPa, porosity $\phi_{bg} = 0.1$, and permeability $\kappa_b = 10^{-4}$ mD (10^{-19} m^2). The fractures and the embedding background are fully saturated with water, with bulk modulus K_f and viscosity η of 2.25 GPa and 0.001 Pa.s, respectively. The fractures have elliptical shapes in the x-y plane, and they are represented with a highly porous and permeable material, with a major axis (length) d_c of approximately 4 cm and a minor axis (aperture) h_c of 0.06 cm. The bulk and shear moduli of the dry porous fracture infill material, K_c and μ_c, are 0.04 and 0.02 GPa, respectively, which are obtained from a drained normal compliance η_N of 10^{-11} m/Pa and a shear compliance η_T of 3×10^{-11} m/Pa for a compliant fracture in a "typical" sandstone (Nakagawa and Schoenberg, 2007). The permeability κ_c of this highly porous infill material is taken to be 100 D (10^{-10} m^2), and its porosity ϕ_{cg} is 0.8. It should be noted that the permeability given here is much lower than that given by the cubic law for the considered fracture parameters (Witherspoon et al., 1980), which is consistent with the fact that fractures are not entirely empty and

their walls are not smooth. We assume that the physical properties of the solid grains composing the fracture infill material are similar to those of the background, thus having the same bulk modulus of 37 GPa.

It should be noted here that, when performing the numerical simulations, the fractures are fully characterized by the physical properties of the infill material described above. However, due to the differences between the geometries of the planar and elliptical fractures, an effective fracture infill material has to be considered when using the theoretical predictions for comparisons with the numerical simulations. To do this, first we compute the normal and tangential excess compliances of the dry fractures, Z_N and Z_T, using equations 22 and 23 with the Eshelby tensor for an elliptical cylinder (infinite height along the z-axis) (shown in Appendix A). Then, the effective elastic properties of the fracture infill material can be calculated using equations 20 and 21. The obtained values are then used in the theoretical predictions of the planar fracture and penny-shaped crack models. The use of these effective properties allows the comparison between the theoretical and numerical results.

It is also important to notice here that, because the dry fracture compliances are related to the elastic properties of the background medium and the material infilling the fractures (equations 22 and 23), the effective elastic properties of the fracture infill material in the theoretical model defined by equations 20 and 21 will depend on the properties of the background and of the fracture infill material.

Furthermore, the specific surface area S of the 2D fractures is also needed in the theoretical predictions and can be obtained according to its definition as follows:

$$S = \frac{4f_c}{\pi h_c}. \tag{41}$$

Using this value of S, the effective distance between the fractures H can also be calculated according to the expression of the specific surface area for the planar fractures ($S = 1/H$). In addition, the fracture density for the 2D sample is defined as follows (e.g., Kachanov and Sevostianov, 2005):

$$\varepsilon = \frac{na^2}{A}, \tag{42}$$

where n is the total fracture number of the 2D sample, a is the major radius of the elliptical 2D fractures, and A is the area of the sample.

Thus, using these properties of the 2D fractures (effective elastic properties, specific surface area, and fracture density), combined with the other known parameters of the sample stated above, the theoretical dispersion and attenuation of the P-wave modulus in the direction perpendicular to the fracture plane c^{sat} (or the component C_{22} in the stiffness matrix of the 2D sample) can be calculated for the three considered fracture geometries (periodic planar fractures, randomly spaced fractures, and penny-shaped cracks).

Results and comparison

Numerical simulation results

Using the numerical upscaling procedure described above and the parameters of the sample, we compute the frequency-dependent stiffness coefficients. Here, we define the variation of the real part as the dispersion of the stiffness cofficients and the absolute value of the ratio of imaginary part to the corresponding real part as the attenuation of the stiffness coefficients. The numerical simulation results show that the coefficients C_{16} and C_{26} are negligibly small compared with the other four coefficients C_{11}, C_{12}, C_{22}, and C_{66}. Thus, we only analyze these four coefficients (C_{11}, C_{12}, C_{22}, and C_{66}), as shown in Figure 3. Because the considered fractures are normal to the y-axis, the dispersion and attenuation for C_{22} are much larger than for the other three coefficients. The values of the other three coefficients keep nearly constant with the frequencies. Their corresponding attenuation is also negligible, especially for C_{11}. Furthermore, it can be clearly seen from C_{22} that the stiffness coefficients reach the low- and high-frequency limits at approximately 10^{-4} and 10 Hz, respectively. The low-frequency limit means that the fluid pressure is uniform throughout the sample, whereas the high-frequency limit indicates that no fluid flow occurs at such frequencies and the fractures are hydraulically

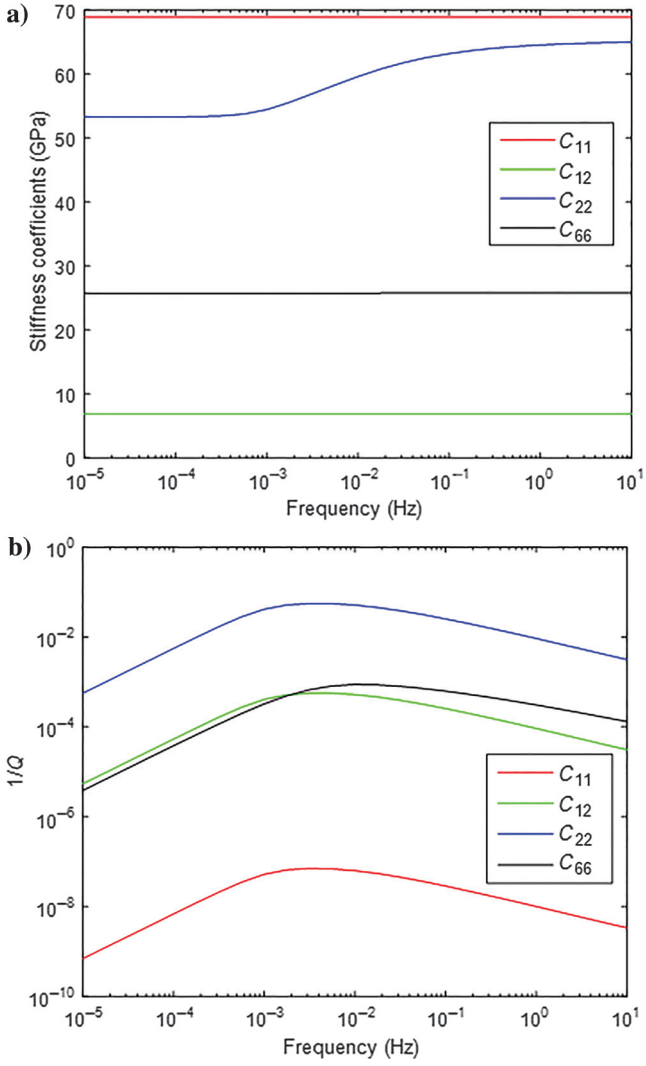

Figure 3. (a) Dispersion and (b) attenuation of the stiffness coefficients given by the numerical simulations for the sample with four parallel fractures.

isolated from the background medium. It should be noted that, because the characteristic frequency for the fluid flow between the fractures and the background medium is proportional to the background permeability (e.g., Gurevich et al., 2009; Guo et al., 2017b), the high frequencies here are actually small compared with the seismic frequency band due to the low background permeability of the sample (10^{-4} mD).

Comparing the shape and characteristic frequency of the attenuation for the four stiffness coefficients, it can be found that they are similar to each other. This is due to the fact that the induced fluid flow between the fractures and the background is normal to the fractures due to its low velocity, and, hence, all the frequency-dependent stiffness coefficients are controlled by the same relaxation function (Krzikalla and Müller, 2011; Galvin and Gurevich, 2015; Kong et al., 2017). For this reason and the fact that the dispersion and attenuation of C_{22} are much higher than those for the other three coefficients, in this paper, we focus on exploring the characteristics of the coefficient C_{22} obtained from the theoretical predictions and numerical simulations. The full stiffness matrix and the anisotropic properties of fractured rocks will be considered in a companion paper.

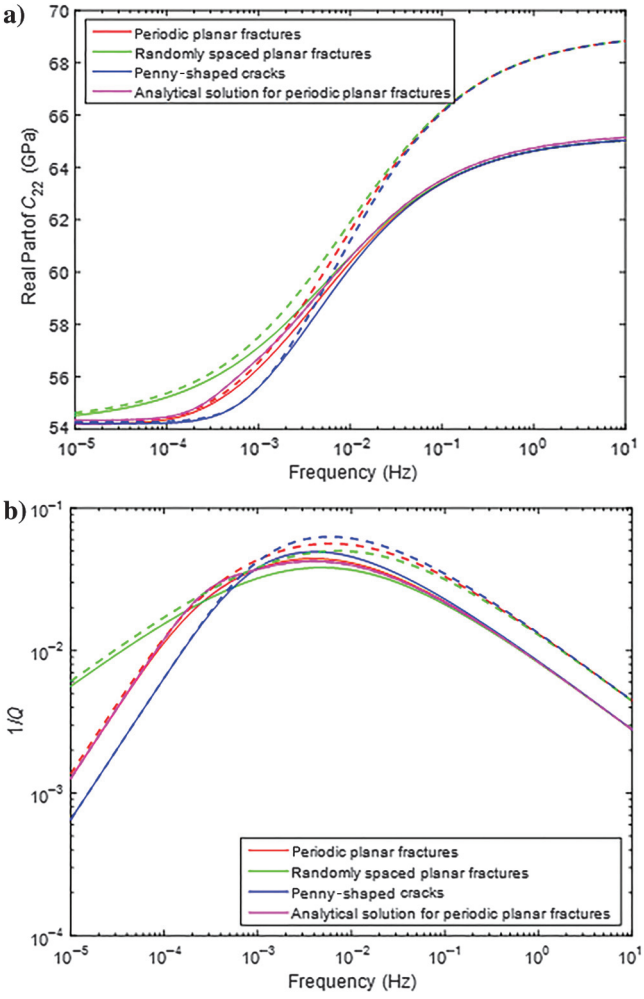

Figure 4. (a) Dispersion and (b) attenuation of C_{22} calculated using the unified model for the sample with four parallel fractures. Note that the solid lines are the results provided by the extended unified model (for fractures with finite thickness), whereas the dashed lines indicate the ones corresponding to the original unified model (for fractures with infinitesimal thickness). To validate the accuracy of the extended unified model, the results given by the analytical solution for the periodic planar fracture case with finite thickness (equation 1) are also shown.

Effects of finite fracture thickness

To analyze the effects of the finite thickness of fractures, we compare the results obtained using the original unified model (considering the fracture thickness as infinitesimal) and the extended unified model (considering the finite fracture thickness effect), as shown in Figure 4. To validate the accuracy of the extended unified model, we also show the results given by the analytical solution for rocks with periodically spaced planar fractures of finite thickness (equation 1). It can be seen that they are almost the same with the corresponding results calculated by the extended unified model proposed in this paper. For the other two types of fractures (randomly spaced planar fractures and penny-shaped cracks), although we do not have the corresponding analytical solutions, the accuracy of the extended unified model can be verified through its relations with the periodic planar fracture case and also by comparison with the numerical simulations in the following section.

For the dispersion of C_{22}, Figure 4a indicates that at low frequencies, the response is not highly sensitive to the finite thickness of the fractures. More in detail, we observe that the infinitesimal fracture thickness model provides slightly higher values of C_{22} compared with those for finite thickness. However, the discrepancies are rather negligible. This is due to the fact that the fracture porosity is small (only 0.0037) and, thus, its contribution to the rock overall porosity is negligible. This, in turn, implies that when using the anisotropic Gassmann's equation to saturate the dry rocks in the low-frequency limit, ignoring this small fracture porosity merely increases the resulting modulus slightly. However, at high frequencies, the situation is drastically different. The influence of this small fracture porosity (or finite fracture thickness) becomes significant, and the values of C_{22} for the infinitesimal fracture thickness models get higher than those corresponding to finite thickness fracture models. The reason is that even a small fracture porosity will result in a nonzero fracture normal compliance in the high-frequency limit, which can significantly decrease the value of C_{22}. Hence, the effects of the small fracture porosity (or the finite fracture thickness) cannot be ignored at high frequencies. In this context, it is important to notice that in the case of low-permeability backgrounds, for frequencies within the seismic band, there is no time for fluid-pressure exchange between this region and the fractures. This implies that the seismic properties are given by the corresponding high-frequency limits, which, according to our results, can be significantly affected by the finite thickness of the fractures. The incapability of the existing models for dealing with these situations may therefore have important implications in the seismic characterization of low-permeability reservoirs containing fractures.

A comparison of the attenuation of C_{22} given by the theoretical models with and without considering the finite fracture thickness effects is shown in Figure 4b. We observe that the influence of the finite fracture thickness on attenuation at low frequencies is small for all the fracture types considered, which is consistent with the observations of Galvin and Gurevich (2009). However, at high frequencies, the attenuation for finite thickness fractures is lower than that for infinitely thin fractures, which is consistent with

the lower dispersion of C_{22} at high frequencies observed for fractures of finite thickness (Figure 4a). It is important to note that the attenuation for the three types of fractures merge together at high frequencies (Figure 4b). This is due to the fact that the energy dissipation at high frequencies only occurs in the immediate vicinity of the fracture surfaces. For the three types of fractures considered in the extended unified model, we use the same specific fracture surface area obtained from the real fracture geometry of the sample (equation 41). Hence, the attenuation for the three types of fractures becomes the same at high frequencies. In summary, the finite fracture thickness has small influence on the dispersion and attenuation of the stiffness coefficients of fractured rocks at low frequencies. However, this effect becomes significant at high frequencies.

Theoretical predictions versus numerical simulations

To compare the theoretical predictions of the extended model and the results of the numerical simulations, we consider two cases that have low and relatively high fracture densities, respectively (Figure 2). For the low fracture density case, we use the sample with four regularly distributed parallel fractures, which has a fracture density of 0.06. The properties of this sample are presented above. For the high fracture density case, we consider a set of samples that have dimensions of 20×20 cm and contain 20 parallel fractures randomly distributed. Each sample corresponds to one realization of a random fracture distribution of interest (Figure 2b). By considering 20 realizations of the random fracture distributions in the numerical simulations, the standard deviations of the P-wave moduli C_{22} as functions of the number of realizations become nearly constant at the low and high frequencies. Hence, we can take the mean value of the P-wave moduli C_{22} of these 20 samples to represent the results of numerical simulations for the random fracture distribution case with relatively high fracture density (0.20). The other properties of these samples remain the same as for the sample with four parallel fractures. This case allows us to study the influence of fracture interactions on the seismic signatures as well as the applicability of the extended model under high fracture density conditions.

The results of the numerical simulations and the theoretical predictions are shown in Figure 5. It is found that the theoretical predictions given by the penny-shaped crack model match the numerical simulation results best for both cases. This is expected because the shape of the 2D cracks is closer to that of penny-shaped cracks. At high frequencies, good agreement can be found between the theoretical predictions of the penny-shaped crack model and the numerical simulations, even for the case with 20 fractures. However, we observe some small discrepancies at low frequencies, which are probably due to fracture interactions. This is supported by the normal stress distributions computed in the low- and high-frequency limits (approximately 10^{-4} and 10 Hz, respectively) in response to the vertical numerical relaxation test, as shown in Figure 6 for the sample with four fractures. In the low-frequency limit, we can observe some overlap between the stress shielding zones (blue) of adjacent fractures, indicating the interactions between the fractures. However, in the high-frequency limit, due to the diminished stiffness contrast between background and fractures, the overlap between the stress shielding zones tends to vanish, and therefore, there are nearly no interactions between the fractures. This result conforms with the findings of Milani et al. (2016). Thus, we can see the good agreement between the theoretical predictions

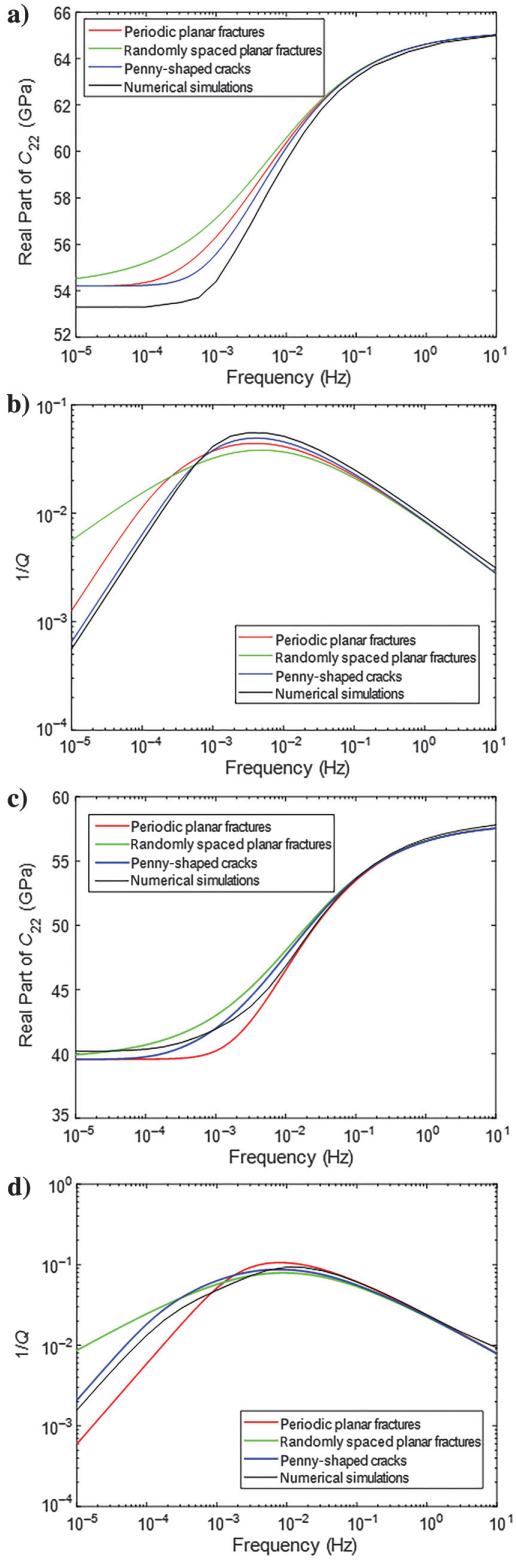

Figure 5. Numerical simulation results of dispersion and attenuation of C_{22} and those predicted by the extended theoretical models. Panels (a) and (b) show the dispersion and attenuation, respectively, for the case with low fracture density (the sample with four parallel fractures), whereas Panels (c) and (d) include the corresponding results for the case with high fracture density (mean value of 20 realizations of samples with 20 randomly-distributed parallel fractures).

and the numerical simulations at high frequencies, but some small discrepancies are observed at low frequencies.

It can be noticed that, even for the case with relatively high fracture density (0.20), the discrepancies between the theoretical predictions and the numerical simulations are small. Indeed, Grechka and Kachanov (2006) carry out several numerical simulations for rocks with dense fracture densities and compared the results with the noninteractive theoretical approach to study the effects of fracture interactions. They find that, in rocks with random distributions of fractures, the influence of fracture interactions is rather small due to the cancellation of the competing effects of stress shielding and amplification. This implies that the noninteractive approach is still valid even for rocks with relatively high fracture densities. For the case with relatively high fracture density (0.20) investigated in this paper, due to the random distribution of the fractures, the stress shielding and amplification effects can be effectively canceled out, which results in the overall good agreement observed between the theoretical predictions of the noninteractive penny-shaped crack model and the numerical simulation results.

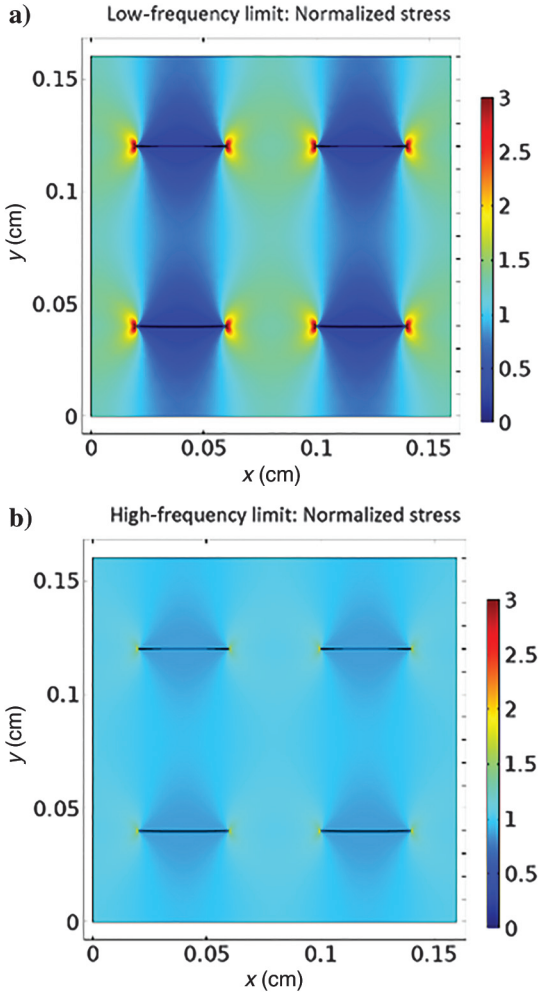

Figure 6. Spatial distribution of the real part of the normal stress in response to the vertical numerical relaxation test for the sample with four fractures. The upper and lower panels correspond to the low- and high-frequency limits (approximately 10^{-4} and 10 Hz), respectively. The values are normalized by the average stress and, hence, values smaller than one represent stress shielding and those larger than one represent stress amplification.

CONCLUSION

The objective of this work was to improve the applicability of theoretical models in the prediction of seismic dispersion and attenuation in reservoirs with aligned fractures. To do so, we extended the existing unified theoretical model for three fracture types, namely, periodically and randomly distributed planar fractures and penny-shaped cracks, to the case of finite fracture thickness for P-waves propagating perpendicular to the fracture plane. In addition, we carried out numerical simulations to explore the validity of the extended unified theoretical model for given fracture configurations. Two 2D rock samples with aligned fractures were studied, one with low fracture density (0.06) and the other with relatively high fracture density (0.20). The results show that the influence of fracture thickness on seismic dispersion and attenuation is rather small at low frequencies. However, it gets significant at high frequencies. This is an important result that should be taken into account when characterizing low-permeability formations containing fractures, for which the seismic properties typically correspond to the high-frequency limit of the involved WIFF mechanism.

Comparing theoretical predictions of the extended models with the corresponding numerical simulations, it is found that the penny-shaped model matches the numerical simulation results best. Furthermore, the study indicates that this theoretical model is applicable even in the case of rocks with relatively high fracture density. Analyses of stress distributions in response to numerical vertical relaxation tests suggest that the small discrepancies observed between the theoretical predictions and the numerical simulations are probably due to fracture interactions.

Due to the very high computational cost of 3D numerical simulations, in this paper, we compared the predictions of a 3D theoretical model with 2D numerical results. However, the current computational capabilities allow us to consider the simple case of a regular distribution of penny-shaped cracks embedded in a 3D sample. In this case, we observe good agreement between the theoretical predictions and the numerical simulations, which suggests the applicability of the theoretical model in the 3D context. An exhaustive 3D analysis will be carried out in the future with improved computational capabilities. Moreover, the good agreement of our 3D theoretical model with the results of the 2D numerical simulations itself has indicated the robustness of the former. This implies the wide application scope of our theoretical model in the context of seismic characterization of fractured reservoirs.

ACKNOWLEDGMENTS

The authors are grateful to the sponsors of the Curtin Reservoir Geophysics Consortium (CRGC) for the financial support.

APPENDIX A

ESHELBY TENSOR

The Eshelby tensor S_{mnkl} for an ellipsoidal inclusion embedded in an infinite elastic background can be found in Mura (1987, section 11, page 80), which was derived by Eshelby (1957). Assuming the radii of the ellipsoidal inclusion along the x-, y-, and z-axes are

a_1, a_2, and a_3, respectively, and the Poisson's ratio of the elastic background is ν, the Eshelby tensor for elliptic cylinder ($a_3 \to \infty$) and penny-shaped cracks ($a_1 = a_2 \gg a_3$) are as follows:

Elliptic cylinders ($a_3 \to \infty$):

$$S_{1111} = \frac{1}{2(1-\nu)}\left\{\frac{a_2^2 + 2a_1a_2}{(a_1+a_2)^2} + (1-2\nu)\frac{a_2}{a_1+a_2}\right\}, \tag{A-1}$$

$$S_{2222} = \frac{1}{2(1-\nu)}\left\{\frac{a_1^2 + 2a_1a_2}{(a_1+a_2)^2} + (1-2\nu)\frac{a_1}{a_1+a_2}\right\}, \tag{A-2}$$

$$S_{3333} = 0, \tag{A-3}$$

$$S_{1122} = \frac{1}{2(1-\nu)}\left\{\frac{a_2^2}{(a_1+a_2)^2} - (1-2\nu)\frac{a_2}{a_1+a_2}\right\}, \tag{A-4}$$

$$S_{2233} = \frac{1}{2(1-\nu)}\frac{2\nu a_1}{a_1+a_2}, \tag{A-5}$$

$$S_{3311} = 0, \tag{A-6}$$

$$S_{1133} = \frac{1}{2(1-\nu)}\frac{2\nu a_2}{a_1+a_2}, \tag{A-7}$$

$$S_{2211} = \frac{1}{2(1-\nu)}\left\{\frac{a_1^2}{(a_1+a_2)^2} - (1-2\nu)\frac{a_1}{a_1+a_2}\right\}, \tag{A-8}$$

$$S_{3322} = 0, \tag{A-9}$$

$$S_{1212} = \frac{1}{2(1-\nu)}\left\{\frac{a_1^2 + a_2^2}{2(a_1+a_2)^2} + \frac{1-2\nu}{2}\right\}, \tag{A-10}$$

$$S_{2323} = \frac{a_1}{2(a_1+a_2)}, \tag{A-11}$$

$$S_{3131} = \frac{a_2}{2(a_1+a_2)}. \tag{A-12}$$

For the other components, they can be obtained by using the following relations:

$$S_{mnkl} = S_{nmkl} = S_{mnlk}. \tag{A-13}$$

Penny-shaped cracks ($a_1 = a_2 \gg a_3$)

$$S_{1111} = S_{2222} = \frac{13-8\nu}{32(1-\nu)}\pi\frac{a_3}{a_1}, \tag{A-14}$$

$$S_{3333} = 1 - \frac{1-2\nu}{1-\nu}\frac{\pi}{4}\frac{a_3}{a_1}, \tag{A-15}$$

$$S_{1122} = S_{2211} = \frac{8\nu-1}{32(1-\nu)}\pi\frac{a_3}{a_1}, \tag{A-16}$$

$$S_{1133} = S_{2233} = \frac{2\nu-1}{8(1-\nu)}\pi\frac{a_3}{a_1}, \tag{A-17}$$

$$S_{3311} = S_{3322} = \frac{\nu}{1-\nu}\left(1 - \frac{4\nu+1}{8\nu}\pi\frac{a_3}{a_1}\right), \tag{A-18}$$

$$S_{1212} = \frac{7-8\nu}{32(1-\nu)}\pi\frac{a_3}{a_1}, \tag{A-19}$$

$$S_{1313} = S_{2323} = \frac{1}{2}\left(1 + \frac{\nu-2}{1-\nu}\frac{\pi}{4}\frac{a_3}{a_1}\right). \tag{A-20}$$

The other components can be obtained using equation A-13. For the other specific shapes, the corresponding Eshelby tensor is given in Mura (1987, section 11, page 80).

REFERENCES

Abdassah, D., and I. Ershaghi, 1986, Triple-porosity systems for representing naturally fractured reservoirs: SPE Formation Evaluation, **1**, 113–127, doi: 10.2118/13409-PA.

Biot, M. A., 1941, General theory of three-dimensional consolidation: Journal of Applied Physics, **12**, 155–164, doi: 10.1063/1.1712886.

Brajanovski, M., B. Gurevich, and M. Schoenberg, 2005, A model for P-wave attenuation and dispersion in a porous medium permeated by aligned fractures: Geophysical Journal International, **163**, 372–384, doi: 10.1111/j.1365-246X.2005.02722.x.

Brajanovski, M., T. M. Müller, and B. Gurevich, 2006, Characteristic frequencies of seismic attenuation due to wave-induced fluid flow in fractured porous media: Geophysical Journal International, **166**, 574–578, doi: 10.1111/j.1365-246X.2006.03068.x.

Brown, R. J. S., and J. Korringa, 1975, On the dependence of the elastic properties of a porous rock on the compressibility of the pore fluid: Geophysics, **40**, 608–616, doi: 10.1190/1.1440551.

Carcione, J., 2001, Wave fields in real media: Wave propagation in anisotropic, inelastic and porous media: Pergamon.

Chapman, M., 2003, Frequency dependent anisotropy due to mesoscale fractures in the presence of equant porosity: Geophysical Prospecting, **51**, 369–379, doi: 10.1046/j.1365-2478.2003.00384.x.

Chapman, M., E. Liu, and X.-Y. Li, 2006, The influence of fluid-sensitive dispersion and attenuation on AVO analysis: Geophysical Journal International, **167**, 89–105, doi: 10.1111/j.1365-246X.2006.02919.x.

Chapman, M., S. V. Zatsepin, and S. Crampin, 2002, Derivation of a microstructural poroelastic model: Geophysical Journal International, **151**, 427–451, doi: 10.1046/j.1365-246X.2002.01769.x.

Cho, Y., O. G. Apaydin, and E. Ozkan, 2013, Pressure-dependent natural-fracture permeability in shale and its effect on shale-gas well production: SPE Reservoir Evaluation & Engineering, **16**, 216–228, doi: 10.2118/159801-PA.

Eshelby, J. D., 1957, The determination of the elastic field of an ellipsoidal inclusion, and related problems: Proceedings of the Royal Society A: Mathematical, Physical and Engineering Sciences, **241**, 376–396, doi: 10.1098/rspa.1957.0133.

Gale, J. F. W., S. E. Laubach, J. E. Olson, P. Eichhubl, and A. Fall, 2014, Natural fractures in shale: A review and new observations: AAPG Bulletin, **98**, 2165–2216, doi: 10.1306/08121413151.

Galvin, R. J., and B. Gurevich, 2006, Interaction of an elastic wave with a circular crack in a fluid-saturated porous medium: Applied Physics Letters, **88**, 061918, doi: 10.1063/1.2165178.

Galvin, R. J., and B. Gurevich, 2007, Scattering of a longitudinal wave by a circular crack in a fluid-saturated porous medium: International Journal of Solids and Structures, **44**, 7389–7398, doi: 10.1016/j.ijsolstr.2007.04.011.

Galvin, R. J., and B. Gurevich, 2009, Effective properties of a poroelastic medium containing a distribution of aligned cracks: Journal of Geophysical Research, **114**, B07305, doi: 10.1029/2008JB006032.

Galvin, R. J., and B. Gurevich, 2015, Frequency-dependent anisotropy of porous rocks with aligned fractures: Geophysical Prospecting, **63**, 141–150, doi: 10.1111/1365-2478.12177.

Gassmann, F., 1951, Über die Elastizität poröser Medien: Vierteljahresschrift der Naturforschenden Gesellschaft in Zürich, **96**, 1–23.

Grechka, V., and M. Kachanov, 2006, Effective elasticity of rocks with closely spaced and intersecting cracks: Geophysics, **71**, no. 3, D85–D91, doi: 10.1190/1.2197489.

Guo, J., J. G. Rubino, N. D. Barbosa, S. Glubokovskikh, and B. Gurevich, 2017a, Seismic dispersion and attenuation in saturated porous rocks with aligned fractures of finite thickness: Theory and numerical simulations — Part II: Frequency-dependent anisotropy: Geophysics, **83**, this issue, doi: 10.1190/geo2017-0066.1.

Guo, J., J. G. Rubino, S. Glubokovskikh, and B. Gurevich, 2017b, Effects of fracture intersections on seismic dispersion: Theoretical predictions versus numerical simulations: Geophysical Prospecting, **65**, 1264–1276, doi: 10.1111/1365-2478.12474.

Gurevich, B., 2003, Elastic properties of saturated porous rocks with aligned fractures: Journal of Applied Geophysics, **54**, 203–218, doi: 10.1016/j.jappgeo.2002.11.002.

Gurevich, B., M. Brajanovski, R. J. Galvin, T. M. Müller, and J. Toms-Stewart, 2009, P-wave dispersion and attenuation in fractured and porous reservoirs: Poroelasticity approach: Geophysical Prospecting, **57**, 225–237, doi: 10.1111/j.1365-2478.2009.00785.x.

Gurevich, B., and S. L. Lopatnikov, 1995, Velocity and attenuation of elastic waves in finely layered porous rocks: Geophysical Journal International, **121**, 933–947, doi: 10.1111/j.1365-246X.1995.tb06449.x.

Hudson, J. A., E. Liu, and S. Crampin, 1996, The mechanical properties of materials with interconnected cracks and pores: Geophysical Journal International, **124**, 105–112, doi: 10.1111/j.1365-246X.1996.tb06355.x.

Jakobsen, M., 2004, The interacting inclusion model of wave-induced fluid flow: Geophysical Journal International, **158**, 1168–1176, doi: 10.1111/j.1365-246X.2004.02360.x.

Jakobsen, M., and J. A. Hudson, 2003, Visco-elastic waves in rock-like composites: Studia Geophysica et Geodaetica, **47**, 793–826, doi: 10.1023/A:1026394819263.

Jakobsen, M., T. A. Johansen, and C. McCann, 2003, The acoustic signature of fluid flow in complex porous media: Journal of Applied Geophysics, **54**, 219–246, doi: 10.1016/j.jappgeo.2002.11.004.

Johnson, D. L., 2001, Theory of frequency dependent acoustics of patchy-saturated porous media: The Journal of the Acoustical Society of America, **110**, 682–694, doi: 10.1121/1.1381021.

Kachanov, M., and I. Sevostianov, 2005, On quantitative characterization of microstructures and effective properties: International Journal of Solids and Structures, **42**, 309–336, doi: 10.1016/j.ijsolstr.2004.06.016.

Kazemi, H., L. S. Merrill, Jr., K. L. Porterfield, and P. R. Zeman, 1976, Numerical simulation of water-oil flow in naturally fractured reservoirs: SPE Journal, **16**, 317–326, doi: 10.2118/5719-PA.

Kong, L., B. Gurevich, Y. Zhang, and Y. Wang, 2017, Effect of fracture fill on frequency dependent anisotropy of fractured porous rocks: Geophysical Prospecting, **65**, 1649–1661, doi: 10.1111/1365-2478.12505.

Krzikalla, F., and T. Müller, 2011, Anisotropic P-SV-wave dispersion and attenuation due to inter-layer flow in thinly layered porous rocks: Geophysics, **76**, no. 3, WA135–WA145, doi: 10.1190/1.3555077.

Lambert, G., B. Gurevich, and M. Brajanovski, 2006, Attenuation and dispersion of P-waves in porous rocks with planar fractures: Comparison of theory and numerical simulation: Geophysics, **71**, no. 3, N41–N45, doi: 10.1190/1.2197490.

Liu, C., and Y. Abousleiman, 2016, N-porosity and N-permeability generalized wellbore stability analytical solutions and applications: 50th US Rock Mechanics/Geomechanics Symposium, ARMA, 16–417.

Liu, C., A. Mehrabian, and Y. Abousleiman, 2017, Poroelastic dual-porosity/dual-permeability after-closure pressure-curves analysis in hydraulic fracturing: SPE Journal, **22**, 198–218, doi: 10.2118/181748-PA.

Maultzsch, S., M. Chapman, E. Liu, and X.-Y. Li, 2003, Modeling frequency-dependent seismic anisotropy in fluid-saturated rock with aligned fractures: Implication of fracture size estimation from anisotropic measurements: Geophysical Prospecting, **51**, 381–392, doi: 10.1046/j.1365-2478.2003.00386.x.

Maultzsch, S., M. Chapman, E. Liu, and X.-Y. Li, 2007, Modeling and analysis of attenuation anisotropy in multi-azimuth VSP data from the Clair field: Geophysical Prospecting, **55**, 627–642, doi: 10.1111/j.1365-2478.2007.00645.x.

Milani, M., J. G. Rubino, T. M. Müller, B. Quintal, E. Caspari, and K. Holliger, 2016, Representative elementary volumes for evaluating effective seismic properties of heterogeneous poroelastic media: Geophysics, **81**, no. 2, D169–D181, doi: 10.1190/geo2015-0173.1.

Müller, T. M., and E. Rothert, 2006, Seismic attenuation due to wave-induced flow: Why Q in random structures scales differently: Geophysical Research Letters, **33**, L16305, doi: 10.1029/2006GL026789.

Mura, T., 1987, Micromechanics of defects in solids: Martinus Nijhoff Publishers.

Nakagawa, S., and M. A. Schoenberg, 2007, Poroelastic modeling of seismic boundary conditions across a fracture: The Journal of the Acoustical Society of America, **122**, 831–847, doi: 10.1121/1.2747206.

Nelson, R. A., 2001, Geologic analysis of naturally fractured reservoirs: Gulf Professional Publishing.

Norris, A. N., 1993, Low-frequency dispersion and attenuation in partially saturated rocks: The Journal of the Acoustical Society of America, **94**, 359–370, doi: 10.1121/1.407101.

Nye, J. F., 1985, Physical properties of crystals: Their representation by tensors and matrices: Oxford University Press.

Pérez, M. A., V. Grechka, and R. J. Michelena, 1999, Fracture detection in a carbonate reservoir using a variety of seismic methods: Geophysics, **64**, 1266–1276, doi: 10.1190/1.1444633.

Pride, S. R., and J. G. Berryman, 2003, Linear dynamics of double-porosity and dual-permeability materials. II: Fluid transport equations: Physical Review E, **68**, 036604, doi: 10.1103/PhysRevE.68.036604.

Questiaux, J.-M., G. D. Couples, and N. Ruby, 2010, Fractured reservoirs with fracture corridors: Geophysical Prospecting, **58**, 279–295, doi: 10.1111/j.1365-2478.2009.00810.x.

Rubino, J. G., E. Caspari, M. Milani, T. M. Müller, and K. Holliger, 2015, Seismic anisotropy in fractured low-permeability formations: The effects of hydraulic connectivity: 85th Annual International Meeting, SEG, Expanded Abstracts, 3219–3223.

Rubino, J. G., E. Caspari, T. M. Müller, M. Milani, N. D. Barbosa, and K. Holliger, 2016, Numerical upscaling in 2D heterogeneous poroelastic rocks: Anisotropic attenuation and dispersion of seismic waves: Journal of Geophysical Research, **121**, 6698–6721.

Rubino, J. G., T. M. Müller, L. Guarracino, M. Milani, and K. Holliger, 2014, Seismoacoustic signatures of fractures connectivity: Journal of Geophysical Research: Solid Earth, **119**, 2252–2271, doi: 10.1002/2013JB010567.

Rubino, J. G., C. L. Ravazzoli, and J. E. Santos, 2009, Equivalent viscoelastic solids for heterogeneous fluid-saturated porous rocks: Geophysics, **74**, no. 1, N1–N13, doi: 10.1190/1.3008544.

Schoenberg, M., 1980, Elastic wave behavior across linear slip interfaces: Journal of the Acoustical Society of America, **68**, 1516–1521.

Schoenberg, M., and J. Douma, 1988, Elastic wave propagation in media with parallel fractures and aligned cracks: Geophysical Prospecting, **36**, 571–590, doi: 10.1111/j.1365-2478.1988.tb02181.x.

Schoenberg, M., and C. M. Sayers, 1995, Seismic anisotropy of fractured rock: Geophysics, **60**, 204–211, doi: 10.1190/1.1443748.

Sevostianov, I., and M. Kachanov, 1999, Compliance tensors of ellipsoidal inclusions: International Journal of Fractures, **96**, 3–7, doi: 10.1023/A:1018712913071.

Wenzlau, F., J. B. Altmann, and T. M. Müller, 2010, Anisotropic dispersion and attenuation due to wave-induced fluid flow: Quasi-static finite element modeling in poroelastic solids: Journal of Geophysical Research, **115**, B07204, doi: 10.1029/2009JB006644.

White, J. E., N. G. Mikhaylova, and F. M. Lyakhovitsky, 1975, Low-frequency seismic waves in fluid-saturated layered rocks: Izvestiya, Physics of the Solid Earth, **11**, 654–659.

Witherspoon, P. A., J. S. Y. Wang, K. Iwai, and J. E. Gale, 1980, Validity of cubic law for fluid flow in a deformable rock fracture: Water Resources Research, **16**, 1016–1024, doi: 10.1029/WR016i006p01016.